A Spatial Regulated Patch-Wise Approach for Cervical Dysplasia Diagnosis

Ying Zhang[1],[2],**Yifang Yin**[1*], **Zhenguang Liu**[3*], **Roger Zimmermann**[1]
[1]School of Computing, National University of Singapore
[2]School of Computer Science, Northwestern Polytechnical University
[3] School of Computer and Information Engineering, Zhejiang Gongshang University
{dcszyi, idsyin, dcsrz}@nus.edu.sg, liuzhenguang2008@gmail.com

Abstract

Cervical dysplasia diagnosis via visual investigation is a challenging problem. Recent approaches use deep learning techniques to extract features and require the downsampling of high-resolution cervical screening images to smaller sizes for training. Such a reduction may result in the loss of visual details that appear weakly and locally within a cervical image. To overcome this challenge, our work divides an image into patches and then represents it from patch features. We aggregate patch patterns into an image feature in a weighted manner by considering the patch–image relationship. The weights are visualized as a heatmap to explain where the diagnosis results come from. We further introduce a spatial regulator to guide the classifier to focus on the cervix region and to adjust the weight distribution, without requiring any manual annotations of the cervix region. A novel iterative algorithm is designed to refine the regulator, which is able to capture the variations in cervix center locations and shapes. Experiments on an 18-year real-world dataset indicate a minimal of 3.47%, 4.59%, 8.54% improvements over the state-of-the-art in accuracy, F1, and recall measures, respectively.

Introduction

Cervical cancer ranks fourth among the most frequent cancers in women and WHO reports approximately 90% of its deaths occur in less developed countries. However, statistics show that cervical cancer is more than 90% treatable if it is detected at an early stage (Gotlieb et al. 2017). An abnormality might be identified by cervical intraepithelial neoplasia (CIN) which is the precancerous change and abnormal growth of squamous cells on the surface of the cervix (Kumar V 2007). There exist a few screening methods to diagnose cervical dysplasia including but not limited to, a Pap smear test, an HPV test, and visual examinations. The first two are conducted in a laboratory setting and require professional medical devices as well as highly trained experts. Thus, they might not be easily deployed in less developed regions or countries where deaths from cervical cancer occur more often. Consequently, performing cost-effective and non-invasive visual screening shows great potential in the medical field (Do et al. 2018; Feng and Zhou 2016). In a visual inspection, a non-physician takes colposcopic photographs of the cervix after the application of 5% acetic acid (VIA) to the cervix epithelium and submits them to a physician for further interpretation if certain visual characteristics appear. In this paper, the cervical images refer to the colposcopic photographs taken by the VIA approach.

Naturally, visual inspection lends itself to a conversion of the cervical dysplasia diagnosis problem into a binary image classification, solvable by computer. The CIN grades 0 and 1 are labeled as normal while CIN 2+ identifies abnormal cases. The cervical images have a few challenging characteristics. (1) They are usually of high resolution. (2) In a majority of cases the images contains a large amount of irrelevant background as the non-cervix tissues or medical instruments (Gordon et al. 2006). (3) The transformation zone, the most common area on the cervix for abnormal cells to develop, takes up a relatively small fraction of the full image. (4) The correlation between the visual clues of abnormal tissues and CIN grades is relatively weak (Xu et al. 2017). Thus, it is not very effective to directly import the full images into modern classification models as the heavy compression might lead to a loss of the weak visual details of the abnormal tissue (Zhou, Zhang, and Wu 2018) and the small part of cervical lesion results in information bias (Xue, Ng, and Qiao 2020). To alleviate some of these challenges, nearly all conventional approaches manually label a tight bounding box of the cervical region or even the transformation zone and crop it for further examination (Xu et al. 2017; Hu et al. 2019; Liu et al. 2013). However, such manual labeling is not always available and its quality strongly depends on the subjective experience of annotators (Xue, Ng, and Qiao 2020). Different from such approaches, this paper proposes a method that does not require such manual annotations but instead automatically focuses on the proper region of interest (ROI) for detection.

The proposed framework is illustrated in Fig. 1. Each image is divided into sub-regions (patches), from which the image-level features will eventually be reassembled and trained together with the labels in a supervised manner. The model leverages three sets of information during the training: (1) The *patch visual contents*, which is used to learn the distinguishable local patterns of abnormal tissues. (2) The *patch–image relationship*, which encapsulates that patches should contribute to various image features differently. This

*Corresponding authors

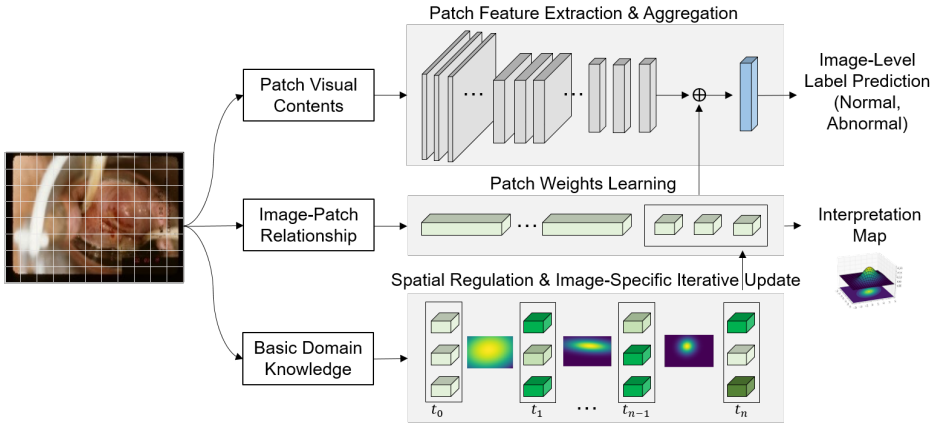

Figure 1: The workflow of our proposed explainable cervical dysplasia diagnosis model. We divide a cervical image into non-overlapping patches and jointly leverage the patch visual contents, image-patch relationship and basic domain knowledge to eventually output an image-level binary label as well as an interpretation map. Patch features are individually extracted and are aggregated to an image-level feature via patch-weights learning by considering the image-patch relationship. Basic domain knowledge is incorporated to further adjust the weights spatial distribution via an temporal iterative algorithm.

is inspired by the fact that patches in the normal cases should be cancer-free and thus their patterns should trigger the detection weakly. (3) *Basic domain knowledge*, the fact that cervical colposcopic images are always taken from the same viewing direction indicates a correlation between certain visual contents and their spatial location. Hence we bring in an additional spatial regulation to guide the weights-learning so that the model can focus more on the foreground regions through a novel iterative algorithm. Finally, all information sets are integrated in the training to output not only a binary label but also an interpretation map. In summary, our main contributions include:

- A patch-wise solution for cervical dysplasia diagnosis is proposed. Patch features capture local visual details and are essential for medical applications where lesions generally cover only a small percentage of the high-resolution screening images. Patch patterns are aggregated into image-features in a weighted manner. Such weights can be visualized as a heatmap to make the diagnosis more explainable.
- A novel spatial regulator is introduced to guide the classifier focus on the cervix region. The training requires no manual ROI annotations. Such a hassle free solution is valuable for professional fields with a limited number of experts. The regulator is refined by a novel image-specific iterative algorithm to capture the data variations.
- We evaluate the approach on an 18-year real-world dataset including 490 non-redundant sessions and observe at least 3.47%, 4.59%, 8.54% improvements over existing approaches in accuracy, F1, and recall scores, respectively.

Related Work

We focus on the existing literature that uses the visual information for detection since other modalities are not always available. The early approaches focus on feature engineering and various color or texture based features are proposed (Li et al. 2007; Kim and Huang 2013; Song et al. 2014). A more recent work (Xu et al. 2017) proposes a combination of the pyramid histogram in LAB color space, HOG and LBP (PLAP-PLAB-PHOG) to further surpass the previous studies. With the quick development of deep learning, the latest studies explore end-to-end feature-learning and observe a better performance. For example, Xu et al. (Xu et al. 2017) use the CaffeNet to outperform existing hand-crafted-features. Other convolutional neural networks have been employed such as the AlexNet (Xu et al. 2016), LeNet (Vasudha and Juneja 2018) and Faster RCNN (Hu et al. 2019). Sato et al. (Sato et al. 2018) designed their own network structure and obtain a validation accuracy of around 50% on an in-house dataset. All the above solutions require a preprocessing stage to manually annotate the small cervix region in the raw screening images and the cropped region is used for analysis. However such manual labeling requires expert knowledge and is very time-consuming so that many solutions cannot be applied to the general un-annotated cervical screening images. On the other hand, most of these techniques (Xu et al. 2017, 2016; Vasudha and Juneja 2018; Sato et al. 2018) output a classification label without explaining how the decisions come from, which restrict them to be applied in hospitals due to trust problem (Gu et al. 2020). In contrast, our approach generates not only a binary label but also an interpretation map and the whole process requires no manual annotation for the cervix-region.

Methodology

In the proposed approach we divide each high-resolution image into same-sized patches which capture more local information, and aim to predict the image-level label (abnormal or normal) from such patch-collections. Mathematically, we denote a set of n images as $\{I_1, I_2, \ldots, I_n\}$ and their binary labels as $\{Y_1, Y_2, \ldots, Y_n\}$. For each label, $Y_i \in \{0, 1\}$

where 1 indicates an abnormal (pre-cancer stage) case and 0 otherwise. For an image I_i containing k patches, we use $X_i = \{x_i^j\}, j = 1 \sim k$ to denote its patch-collection. Each patch occupies a set of non-overlapping image pixels and $\mathcal{L}_i$ denotes all patch-locations for the image I_i.

Baseline Patch Feature Learning & Aggregation An intuitive approach for the patch-wise learning is to extract the individual patch patterns, aggregate them as an image-level features, and pair with an image-level label for binary classification. Patch pattern could be an hand-crafted feature or learned through an end-to-end feature representation model. We adopt the latter one to minimize the manual efforts by using a CNN-based network. Concretely, each image patch goes through a stacked of convolutional layers, followed by non-linear activation functions such as ReLu. Denote the parameters in the non-linear transformation as (w, θ) and the patch features as $g(x|w, \theta)$, then the image feature $\mathrm{f}(I_i)$ is created by aggregating all its patch features as in Eqn. 1.

$$\mathrm{f}(I_i|w, \theta, X_i) = \bigoplus_{x_i^j \in X_i} g(x_i^j|w, \theta) \tag{1}$$

where $\bigoplus$ represents an aggregation operation such as concatenation or average. The network architectures could be adjusted for differently sized patches with details in the experiment section. The image-level features are imported to a classifier to output an image-level prediction probability and the binary label is threshold-determined easily. We use a multilayer perceptron network with two hidden layers and the training objective is to minimize the binary cross-entropy loss across n training examples as in Eqn. 2.

$$L_c = \sum_{i=1}^{n} -(\log(P_i) \cdot Y_i + (1 - \log(P_i)) \cdot (1 - Y_i)) \tag{2}$$

where P_i is the predicted probability that an image I_i is likely to be cervical cancerous.

Patch Weights Learning The above formulation ignores the relationship between image label and patch labels. Actually, for a given cervical screening image, it will be a normal case if and only if all its composed patches are free from abnormal tissue. Assume that we have the ground-truth binary label $y_i^j \in \{0, 1\}$ for each individual patch x_i^j, then the label-relationship between the patches and their corresponding image is represented by the following equation:

$$Y_i = \begin{cases} 0, & \text{iff } \sum y_i^j = 0, \\ 1, & \text{otherwise.} \end{cases} \tag{3}$$

Practically, we do not have the ground truth binary labels for patches so that a patch-level classification is impossible. But such a relationship is still of value to improve the classification as the patch patterns found in the normal (negative) case images should not (or not that much) trigger abnormal (positive) labels whereas the opposite is not true. So we relax the patch labels from a hard binary value (0 or 1) to a soft continuous value (between 0 and 1) and convert the patch-image relationship from the label-level in Eqn. 3 to the feature-level as in Eqn. 4. Specifically, we assume that patches contribute to its corresponding image feature with different weights.

$$\mathrm{f}(I_i|w, \theta, X_i) = \bigoplus_{x_i^j \in X_i} a_i^j \cdot g(x_i^j|w, \theta) \tag{4}$$

where a_i^j denotes the weight for patch x_i^j. This new image-level feature is used to achieve the objective in Eqn. 2.

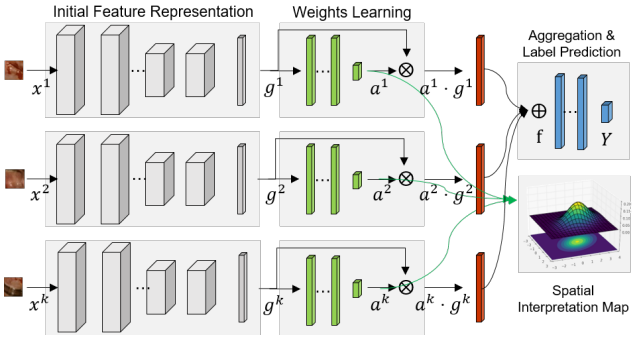

Figure 2: After an initial feature represetntation extraction, we add a weight-learning module so that weighted patch features are aggregated as an image-feature for image-label prediction. The weights naturally form a spatial interpretation map indicating the possible lesion location.

To learn the patch weight, we flatten the initial extracted patch feature and pass it to multiple dense layers. The last single-node layer is activated by Sigmoid function and the activation value is used as the patch weight. Fig. 2 shows this idea. The learnt weights are tied to the patch locations so they naturally composite a heatmap to explain which image subregions are more likely to trigger the final predictions.

Domain-Knowledge Driven Spatial Regulation So far the patch-weights are learnt solely from the patch visual contents but actually some basic domain knowledge could further facilitate a more reasonable patch-weight distribution. In real-world situations, all cervical colposcopic screening images are photographed from an vagina (bottom)-uterus(up) direction. As observed from Fig. 3, when viewed in such an upwards way, the cervix region looks quite like a circular blob-alike region and its center is near the cervix-os, which is the opening in the lower part of the cervix between the uterus and the vagina. Such a blob-alike region covers the transformation zone where cluster most of the abnormal cervical cancer tissues if exist.

This indicates a correlation between some visual contents and their spatial locations in an image. We use such correlation to further regulate the weight distribution so that the training can focus more on the patches within this blob-alike region. Specifically, we introduce a 2D spatial regulator, denoted by S, to indicate the location of the cervical region and propose to learn the key patches in a manner such that they have a good spatial match with the cervix region. As such, another spatial loss is further introduced as below:

$$L_{spatial}(S) = \sum_{i=1}^{n} \sum_{m \in \mathcal{L}_i} D(a_m, s_m) \tag{5}$$

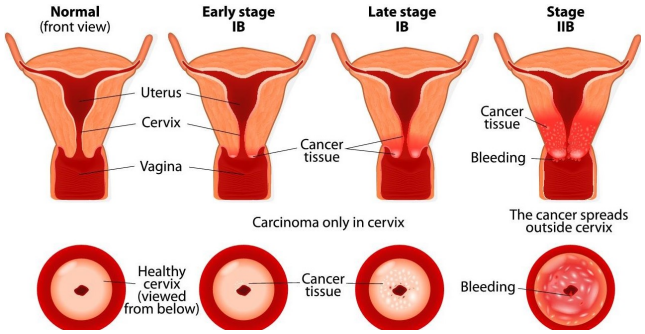

Figure 3: The 2^{nd} row is the upwards view of the cervical region (copyright from Mount Elizabeth Hospital) along different CIN stages. The cervical screening images are all taken from this view. The cervix covers a circular region within the image, and the abnormal tissue, if exists, is mostly spread over this region from cervix-os outwards.

where $\mathcal{L}_i$ records all patch locations in an image and $D(,)$ calculates the dis-similarity between the weight and the spatial regulator by subtracting their dot-product sum by Eqn. 6.

$$D(a,s) = 1 - \frac{a - a_{min}}{a_{max} - a_{min}} \cdot \frac{s - s_{min}}{s_{max} - s_{min}} \tag{6}$$

The overall loss is finalized as a combination of the classification error and the spatial regulation loss as in Eqn. 7.

$$L = \lambda \cdot L_{spatial} + L_c \tag{7}$$

where λ is an adjustable weight. In this work, we test our hypothesis by formulating the spatial regulator as a 2D Gaussian distribution with parameters (μ, σ). Here, μ defines the offset along the horizontal (h) and vertical (v) dimensions and σ is the covariance matrix to define the Gaussian shape.

$$\mu = \begin{bmatrix} \mu_h \\ \mu_v \end{bmatrix} \tag{8}$$

$$\sigma = \begin{bmatrix} \sigma_{hh} & \sigma_{vh} \\ \sigma_{vh} & \sigma_{vv} \end{bmatrix} \tag{9}$$

Based on these two parameters, we can calculate the density value s_m for any location $m \in \mathcal{L}_i$ by Eqn. 10:

$$s_m(\mu, \sigma) = \frac{1}{2\pi|\sigma|^{1/2}} \exp^{(-\frac{1}{2}(m-\mu)^T \sigma^{-1}(m-\mu))} \tag{10}$$

However, such density parameters (μ, θ) are unknown and we will explain in next section how to estimate them accurately for each cervical image.

Image-Specific Iterative Spatial Regulator Estimation To estimate the spatial regulator's parameter, a naïve approach is to choose a pre-defined value according to the prior knowledge and fix it the same for all images. However, such an one-off setting lacks compatibility with various aspects of different cervical images. For example, the cervical region might not always be placed at the image center, or the cervix shape might not be a perfect circle. Thus, instead of using a single and fixed regulator, we design an iterative estimation for each individual image. In particular, for a given epoch at time t and for each individual image, we estimate the image-specific Gaussian parameters from its own patch-weights collections $\{a_m\}, m \in \mathcal{L}_i$ via Maximun Likehihood. Subsequently the image-specific spatial regulator $\hat{S}^t$ is updated based on the estimated Gaussian parameters and will be used to calculate the spatial loss in the next round at time $t+1$. The overall training spatial loss is refined to the following form:

$$L^{t+1} = \lambda \cdot L_{spatial}(\hat{S}^t) + L_c \tag{11}$$

where $\hat{S}^t = \{\hat{S}^t(I_1), \hat{S}^t(I_2), ..., \hat{S}^t(I_n)\}$ contains a collection of refined image-specific spatial regulators.

Algorithm 1: Iterative spatial regulator update.

Result: Regulators S
Initialization: $S_i^0 = G_0$;
for *each training epoch* t **do**
  for *each training image* I_i **do**
    $\{f(x_i^j)\}$ ←Patch feature extraction;
    $\{a_i^j\}$ ←Patch weight learning;
    (μ, σ) ← Parameters estimation from patch weights;
    if (μ, σ) *is valid* **then**
      $\hat{S}^t(I_i)$ ←Update the regulator;
    end
  end
end

Alg.1 summarizes the major steps for the iterative procedure. We initialize each training image's regulator $G_0 = \{\mu, \sigma\}$ to the same values by setting $\mu_h = w_0, \mu_v = h_0, \sigma_{hh} = w_0, \sigma_{vv} = h_0, \sigma_{hv} = 0$, and $\sigma_{vh} = 0$, where w_0 and h_0 are half of the image width and height, respectively. For each image, after patch feature extraction, we learn the patch weights, based on which the parameters of its regulator are estimated. The regulator will be updated if the estimated parameters pass validation by checking if the center location is within the image size. Via such training, the algorithm focuses on the region-of-interests on-the-fly without increasing additional computation complexity.

Experiments

Dataset We evaluate the approach on a real-world database from the U.S. National Cancer Institute (NCI). The dataset is accessible based on request and under constrained agreement. This dataset is from a longitudinal study in Costa Rica: Proyecto Epidemiologico Guanacaste, which is collected over an 18-year period. During this project, each patient may have participated in multiple screening sessions along the whole project timeline. We filter the records that are labeled with ground-truth CIN grades (CIN 0,1,2,3,4) within 1 year of the screening date and in total 978 records are usable for binary classification (non-cancer includes CIN 0,1 and cancer includes CIN 2,3,4). 80% randomly selected data is for training while the remaining 20% is for testing. We keep the ratio between normal/abnormal classes roughly the same between the two parts. Each session may consist of

Model	Annotation	Accuracy	F1	Precision	Recall	AUC ROC	1-EER
Vasudha'18	No	0.7415	0.6923	0.7297	0.6585	0.8143	**0.7895**
Xu'17	No	0.7657	0.7326	0.7	0.7683	0.8049	0.7632
VGG16,FZ1*	No	0.7267	0.6752	0.7067	0.6463	0.775	0.6491
VGG16,FZ2	No	0.7145	0.6581	0.6986	0.622	0.7926	0.7193
VGG16,FZ3	No	0.7082	0.6627	0.6548	0.6707	0.7939	0.7368
VGG16,FZ4	No	0.7318	0.6871	0.6914	0.6829	0.7822	0.7018
InceptionNet	No	0.6049	0.448	0.6512	0.3415	0.6825	0.6491
Hu'19 + AN1500**	Yes	0.5764	0.3455	0.6786	0.2317	0.8145	0.7807
Vasuda'18 + Crop1500ˆ	Yes	0.7737	0.7362	**0.7407**	0.7317	0.8214	0.7807
Xu'17 + Crop1500	Yes	0.7581	0.7134	**0.7467**	0.6829	0.8194	0.7895
VGG16,FZ2 + Crop1500	Yes	0.7518	0.7143	0.6977	0.7317	0.8299	0.7456
Proposed	No	**0.8084**	**0.7821**	0.7216	**0.8537**	**0.8354**	0.7719

*FZn: freeze the lower n blocks of the VGG16. **ANn: annotate center $n \times n$ pixels as cervix bounding box.
ˆCrop$n$: crop the center $n \times n$ pixels as the model inputs.

Table 1: Performance Comparison across Different Approaches.

more than one images which share similar visual contents, so the train/test split is based on sessions for fairness. All images have resolutions around 2400 x 1600. Evaluations includes balanced-accuracy, F1, precision, recall and AUC scores of ROC curve and equal error rate (EER).

Parameters By default, all images are resized to same of 42x42 patches with patch size 28. The feature representation CNN has three convolutional layers with 12, 24, 48 filters and the size of filter is 3×3, followed by ReLu activation and max-pooing. The weights-learning module contains three dense layers of 800, 512, 128 nodes. The aggregated feature is passed to a dense layer activated by Sigmoid. The default parameters are Xavier initialized for all layers. By default, the learning rate is 10^{-5} and λ is 0.1 over a 150-epoch training with early-stop mechanism.

Baselines We compare our model with the following state-of-the arts: 1) **Xu'17** (Xu et al. 2017): it is one of the most active groups working in this field and they use a CaffeNet based transfer learning model to solve the problem which surpassed the best reported hand-crafted feature (around 1% improvement) on the same dataset. We follow their parameter settings and achieve similar results as reported in this paper. 2) **Vasuda'18** (Vasudha and Juneja 2018): it uses the LeNet-based transfer learning but its training and testing data contain the same-session's images so their reported results contains some bias. 3) **VGG16, InceptionNet**. Both above methods are based on transfer-learning so we further test some more recent backbone networks including VGG16 and InceptionNet. VGG16 is much larger than InceptionNet so we freeze different blocks of VGG16 and report the results accordingly. 4) **Hu'19+AN1500** (Hu et al. 2019): We compare a simplified version of this paper that uses RCNN to crop cervix region (ROI) before classification. This model requires additionally experts-labeled ROI ground truth (not available for public) so we cannot fully reproduce it. But as our images are captured in a very controlled environment and the image centers mostly correspond to the ROI, we annotate the center kxk pixels as ROI labels instead. To choose a proper k, we test the traditional transfer-learning models by using the center kxk as input for $k = 900, 1200, 1500$ and observe the size 1500 give the best results. So we choose $k = 1500$ as the annotations to train the RCNN accordingly. Note that this paper (Hu et al. 2019) uses an in-house training dataset 2.4 times patient numbers as ours.

Quantitative Results Table 1 reports the performance on multiple metrics where a few observations are made:

- The proposed method surpasses existing solutions in most scenarios where recall has the largest minimal-increment of 8.54%, followed by F1 of 4.59% and accuracy of 3.47%. In rare-cancer detection, the recall is a very important measurement to avoid missing of a cancerous case. We visualize the approaches' ranking in Fig. 4a.
- The improvement is more obvious comparing to the approaches requiring no cervical region bounding box annotations. This is as expected as cropping out the equipment/environmental content will reduce the background noise. However, a key question is how to select the crop size as a heavy crop may take away useful information while a light crop may be insufficient. This problem is more serious when the data variation is large
- Shallow models (Xu et al. 2017; Vasudha and Juneja 2018) perform better than deep models as VGG16 or InceptionNet. The shallow models focus more on the low-level local clues while the deep models address the high-level global clues. So the performance gap indicates that the local features should be more discriminative than global-features in our problem and this explains the effectiveness of our patch-wise solutions.

ROC Curve Fig. 4b compares the ROC curves among all annotation-free approaches. The closer the curve is to the upper-left corner, the better that approach works. Our model works the best but there is still room for improvements.

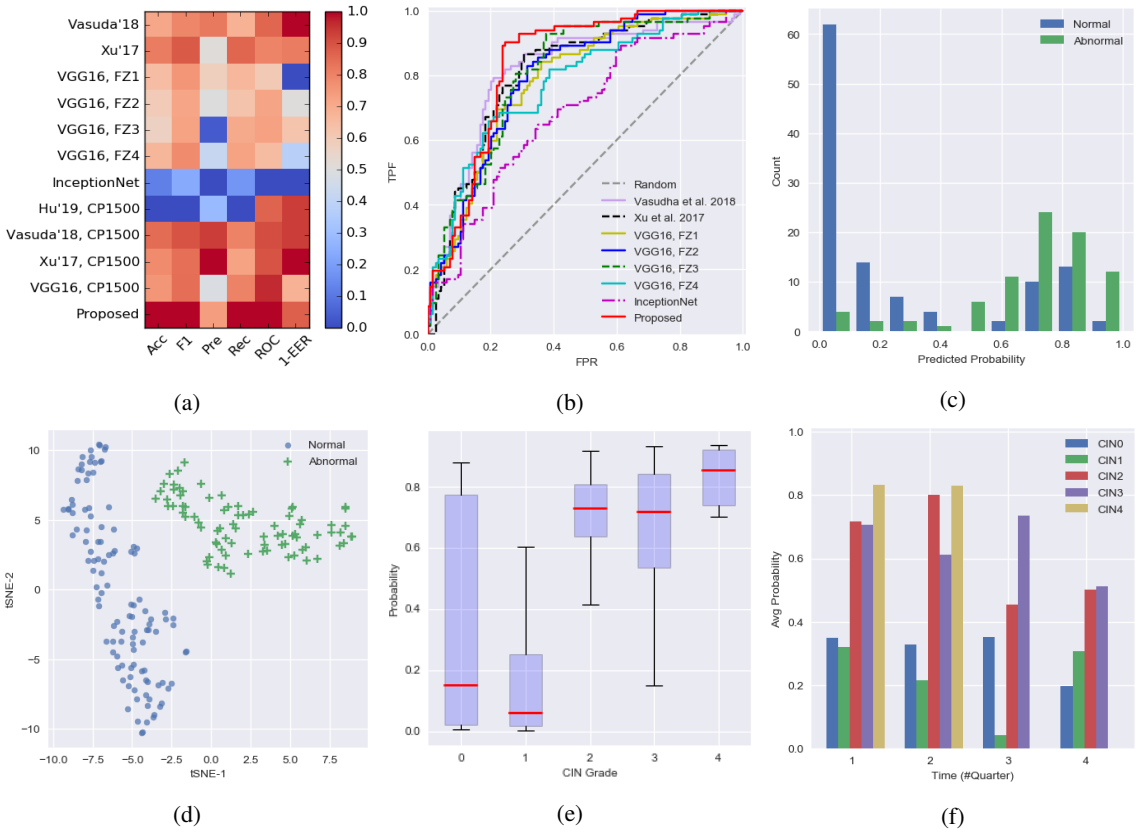

Figure 4: (a) Normalized performance comparison under multiple indicators. (b) ROC curve comparison among approaches require no manual annotations. (c) The predicted probabilities for normal/abnormal data distribute densely at two different ends and this indicates a good binary classification. (d) T-SNE 2D plot of the image-level feature after the proposed patch-feature aggregation and we can see the two classes are clearly separated. (e) Predicted probability statistics for each CIN-grade. (f) Average probability against temporal-stages.

Score Distribution & Feature Visualization Fig. 4c shows the predicted score distribution where the normal (blue) cases are skewed-left while the abnormal (green) ones are skewed right. Such a two-end skewed-distribution suggests an effective classification, which is further validated by the 2D T-SNE plot in Fig. 4d. Points from each category are clustered together while the two clusters are separated.

CIN Grades & Temporal Factor The binary classes (cancer and non-cancer) come from five CIN grades labeled from 0 (normal) to 4 (cancerous), we also analyze the prediction statistics for each category in Fig. 4e. The medium values (the red line in each box), generally go higher along the grade level, indicating a potential possibility for fine-level categorization. Lastly, we discuss the temporal factor influence. Each image is labeled within 1-year from its image-taken date so we divide this 1-year window into four quarters and visualize the average probability in each quarter in Fig. 4f. We have not observed obvious trending and this matches the fact that abnormal cells have the potential to progress to cancer, but may also regress to normal or remain unchanged (Wang et al. 2013).

Interpretability Other than the improvements under standard metrics, our approach has a better interpretability by outputing an additional heatmap from the patch-weights. The first two columns Fig. 5 illustrates a few examples. Column (a) is the screening images and column (b) is the interpretation maps where the bright color indicates the areas where features are mainly learnt from. We can see that they mostly cover the transformation zone within the cervix region. This is an area of changing cells, and it is the most common place on the cervix for abnormal cells to develop.

Impact of Spatial Regulator We remove the spatial regulation module and show the interpretation maps in the column (c) in Fig. 5. The maps are significantly varied from the original maps in column (b) by highlighting mostly the outer background parts which are incorrect. Thus, we surmise that an explainable result might be very important when using computational solutions for cervical dysplasia diagnosis as the doctor can validate the predictions more easily.

Impact of Iterative Algorithm To illustrate the effectiveness of our iterative regulator refinement, we visualize the estimated Gaussian over the temporal dimension in the last four columns of Fig. 5. The yellow color corresponds to the

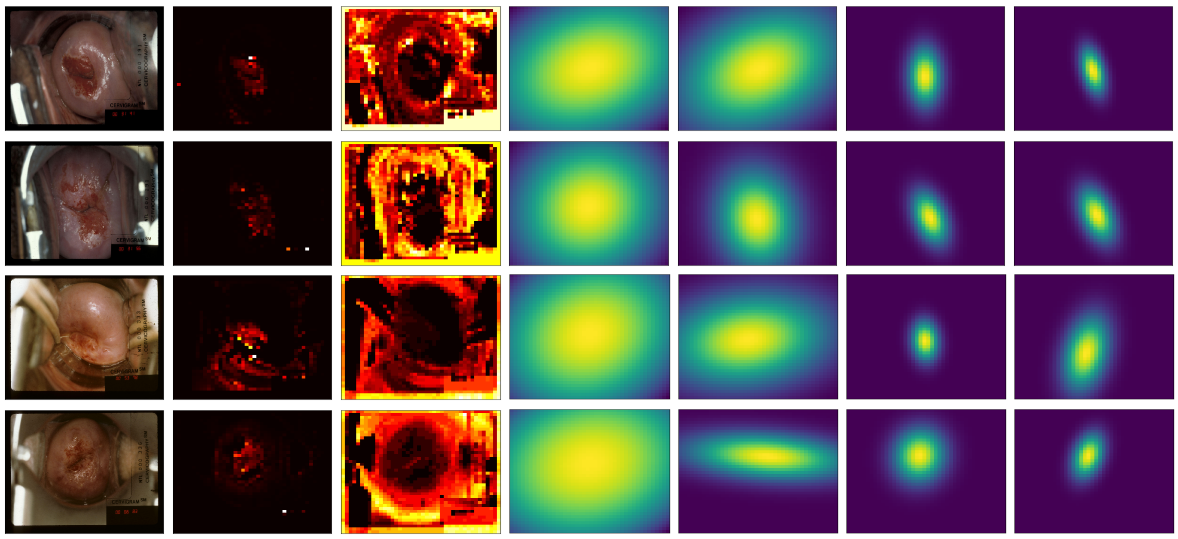

(a) Input (b) Results (c) without the spatial regulation (d) $t = 1$ (e) $t = 32$ (f) $t = 48$ (g) Final

Figure 5: (a) Input cervical images and each row is an example. (b) The final maps where the bright color indicates the features from those regions are more likely to trigger the prediction labels. Our highlights well correspond to the cervix transformation zones. (c) The maps using our model but without spatial regulation and the highlight regions focus more on the background regions. (d-g) These four columns show the refined spatial regulator learnt at epochs 1, 32, 48 and the final one. Via the proposed iterative algorithm, we can see that the regulator gradually changes in locations, sizes and shapes until a good fit to the cervix.

Gaussian center. The updates are reflected in e.g., the cervix shape, the center location, the width-height-ratio and the rotation perspectives. 1) Location-wise, the highlighted areas are gradually shifted to the cervical central area for each individual image through the training. 2) Size-wise, the spread of the Gaussian is gradually converged to a small region. At the very beginning, the Gaussian occupies almost the whole image and it is similar for all examples. After a few steps, the Gaussian focus only on the potential ROI which takes a small ratio over the image. 3) shape-wise, the Gaussian rotates differently for different cases.

	Accuracy	F1	Precision	Recall	ROC
0.5xDefault	0.734	0.687	0.705	0.670	0.789
Default	0.808	0.782	0.721	0.853	0.835
2xDefault	0.791	0.764	0.708	0.829	0.821
4xDefault	0.736	0.701	0.663	0.743	0.765

Table 2: Performance vs. Patch Size.

Impact of Patch Size. Results using different patch sizes (n x Default size) are reported in Table 2. A larger patch size focuses more on the global clues and results a relatively lower performance. This matches the second observations in our quantitative results discussion where a shallow network works better. Another plausible reason might be that a larger patch size will reduce the total number of training patches and this further affect the accuracy eventually.

Conclusion and Future Work

This work proposes a patch-wise solution for cervical cancer image classification. Compared to the majority of solutions in this field which use high-resolution images directly, it has the advantage of retaining local visual details and this is important for medical applications. During the patch feature aggregation, the approach also learns the patch contribution weights, from which an interpretation map is created to indicate which regions mostly trigger the prediction. The framework further integrates basic domain knowledge and introduces an adjustable spatial regulator to control where the classifier should focus on. We have designed a novel iterative training to capture the cervix-image data diversity on-the-fly, so that the variations in terms of center location, size, and rotation are automatically refined for individual images, making the approach more flexible and dynamic. Extensive experiments have been performed to evaluate the approach with significant improvements observed.

In future, we will explore to incorporate some stopping criteria, so that the approach may finalize at a stage to cover a more complete view of the transformation zone. Another direction is to study the effect of various kernels so that the approach can cater to the cervix shape more accurately.

Acknowlegements

This research was supported by the MSIT, Korea, under the ITRC support program (IITP-2020-2020-0-01789) supervised by the IITP. We thank David Levitz and Yonit Zall from MobileODT Ltd. for advise and suggestions.

References

Do, T.-T.; Hoang, T.; Pomponiu, V.; Zhou, Y.; Chen, Z.; Cheung, N.-M.; Koh, D.; Tan, A.; and Tan, S.-H. 2018. Accessible melanoma detection using smartphones and mobile image analysis. *IEEE Transactions on Multimedia* 20(10): 2849–2864.

Feng, Q.; and Zhou, Y. 2016. Kernel combined sparse representation for disease recognition. *IEEE Transactions on Multimedia* 18(10): 1956–1968.

Gordon, S.; Zimmerman, G.; Long, R.; Antani, S.; Jeronimo, J.; and Greenspan, H. 2006. Content analysis of uterine cervix images: initial steps toward content based indexing and retrieval of cervigrams. In *Medical Imaging 2006: Image Processing*, volume 6144, 61444U. International Society for Optics and Photonics.

Gotlieb, A.; Louarn, M.; Nygard, M.; Ruiz-Lopez, T.; Sen, S.; and Gori, R. 2017. Constraint-based verification of a mobile app game designed for nudging people to attend cancer screening. In *IAAI Conference*.

Gu, D.; Li, Y.; Jiang, F.; Wen, Z.; Liu, S.; Shi, W.; Lu, G.; and Zhou, C. 2020. VINet: A Visually Interpretable Image Diagnosis Network. *IEEE Transactions on Multimedia* .

Hu, L.; Bell, D.; Antani, S.; Xue, Z.; Yu, K.; Horning, M. P.; Gachuhi, N.; Wilson, B.; Jaiswal, M. S.; Befano, B.; et al. 2019. An observational study of deep learning and automated evaluation of cervical images for cancer screening. *Journal of the National Cancer Institute* .

Kim, E.; and Huang, X. 2013. A data driven approach to cervigram image analysis and classification. In *Color Medical Image analysis*, 1–13. Springer.

Kumar V, Abbas AK, F. N. M. R. 2007. Robbins Basic Pathology (8th ed.). 718—-721. Elsevier Health Sciences.

Li, W.; Gu, J.; Ferris, D.; and Poirson, A. 2007. Automated image analysis of uterine cervical images. In *Medical Imaging 2007: Computer-Aided Diagnosis*, volume 6514, 65142P. International Society for Optics and Photonics.

Liu, F.; Zhang, Y.; Liu, S.; Zhang, B.; Liu, Q.; Yang, Y.; Luo, J.; Shan, B.; and Bai, J. 2013. Monitoring of tumor response to Au nanorod-indocyanine green conjugates mediated therapy with fluorescence imaging and positron emission tomography. *IEEE transactions on multimedia* 15(5): 1025–1030.

Sato, M.; Horie, K.; Hara, A.; Miyamoto, Y.; Kurihara, K.; Tomio, K.; and Yokota, H. 2018. Application of deep learning to the classification of images from colposcopy. *Oncology letters* 15(3): 3518–3523.

Song, D.; Kim, E.; Huang, X.; Patruno, J.; Muñoz-Avila, H.; Heflin, J.; Long, L. R.; and Antani, S. 2014. Multimodal entity coreference for cervical dysplasia diagnosis. *IEEE transactions on medical imaging* 34(1): 229–245.

Vasudha, A. M.; and Juneja, M. 2018. Cervix Cancer Classification using Colposcopy Images by Deep Learning Method. *International Journal of Engineering Technology Science and Research* .

Wang, S.-M.; Colombara, D.; Shi, J.-F.; Zhao, F.-H.; Li, J.; Chen, F.; Chen, W.; Li, S.-M.; Zhang, X.; Pan, Q.-J.; et al. 2013. Six-year regression and progression of cervical lesions of different human papillomavirus viral loads in varied histological diagnoses. *International Journal of Gynecologic Cancer* 23(4): 716–723.

Xu, T.; Zhang, H.; Huang, X.; Zhang, S.; and Metaxas, D. N. 2016. Multimodal deep learning for cervical dysplasia diagnosis. In *International Conference on Medical Image Computing and Computer-Assisted Intervention*, 115–123. Springer.

Xu, T.; Zhang, H.; Xin, C.; Kim, E.; Long, L. R.; Xue, Z.; Antani, S.; and Huang, X. 2017. Multi-feature based benchmark for cervical dysplasia classification evaluation. *Pattern recognition* 63: 468–475.

Xue, P.; Ng, M. T. A.; and Qiao, Y. 2020. The challenges of colposcopy for cervical cancer screening in LMICs and solutions by artificial intelligence. *BMC Medicine* 18: 1–7.

Zhou, L.; Zhang, C.; and Wu, M. 2018. D-LinkNet: LinkNet With Pretrained Encoder and Dilated Convolution for High Resolution Satellite Imagery Road Extraction. In *CVPR Workshops*, 182–186.